Uniform Large-Area Free-Standing Silver Nanowire Arrays on Transparent Conducting Substrates

Yuyi Feng,[a,*,z] Kwang-Dae Kim,[a] Clayton A. Nemitz,[b] Paul Kim,[c] Thomas Pfadler,[a] Melanie Gerigk,[d] Sebastian Polarz,[d] James A. Dorman,[e] Jonas Weickert,[a] and Lukas Schmidt-Mende[a,z]

[a]*Department of Physics, University of Konstanz, Konstanz 78457, Germany*
[b]*Department of Physics and Astronomy, University of North Carolina, Chapel Hill, North Carolina 27516, USA*
[c]*Chemical Engineering, Yale University, New Haven, Connecticut 06520-0626, USA*
[d]*Department of Chemistry, University of Konstanz, Konstanz 78457, Germany*
[e]*Cain Department of Chemical Engineering, Louisiana State University, Baton Rouge, Louisiana 70803, USA*

Arrays of silver nanowires have received increasing attention in a variety of applications such as surface-enhanced Raman scattering (SERS), plasmonic biosensing and electrode for photoelectric devices. However, until now, large scale fabrication of device-suitable silver nanowire arrays on supporting substrates has seen very limited success. Here we show the synthesis of free-standing silver nanowire arrays on indium-tin oxide (ITO) coated glass by pulsed electrodeposition into anodic aluminum oxide (AAO) templates. We use an in situ oxygen plasma cleaning process and a sputtered Ti layer to enhance the adhesion between the template and ITO glass. An ultrathin gold layer (2 nm) is deposited as a nucleation layer for the electrodeposition of silver. An unprecedented high level of uniformity and control of the nanowire diameter, spacing and length has been achieved. The absorption measurements show that the free-standing silver nanowire arrays possess tunable plasmonic resonances.
 [DOI: 10.1149/2.1141608jes]

Manuscript submitted April 20, 2016; revised manuscript received May 27, 2016. Published June 14, 2016.

Nanowire arrays have attracted much attention in photovoltaic devices,[1–4] sensing,[5,6] plasmonics,[7] surface enhanced Raman scattering,[8] high density data storage,[9] photocatalysts,[10] and nanobiotechnology,[11] due to their unique electrical, optical, magnetic, and chemical properties which are different from those in the bulk state. In photovoltaics nanowire arrays are of particular interest for cost-effective organic and hybrid solar cells, whose near-optimal architecture is proposed to consist of arrays of nanostructures (approximately 200 nm long).[12,13] The major advantage to using nanowire arrays is the enhancement of the charge collection due to the high charge carrier mobility in the metallic and some semiconductor nanowires.[13,14] However, due to the huge junction area, most semiconductor nanowire solar cells face limitations in device performance due to charge recombination across material interfaces,[13,14] leading to poor solar cell performance. Many research groups have tried to address this issue by developing metal oxide core-shell nanowire arrays.[15–17] In this work, a conductive metal oxide core (e.g. ZnO) is coated with a shell layer with an offset conduction band (e.g. TiO_2, Al_2O_3) in order to further increase distance between electron-hole pairs while simultaneously promoting charge extraction along the axis of the nanowire. This phenomenon was further employed in doped TiO_2 core-shell wires to amplify the electron mobility in the core of the wire without forming a recombination center along the internal interface.[18] However, to ultimately enhance the performance of organic solar cells, a hybrid core-shell nanostructure with enhanced charge mobilities could provide an optimal electrode, e.g. a Ag nanowire with an inorganic shell layer. Additionally, these wires promote field amplification via plasmonic resonance as well as acting as a light scatterer,[19] leading to an increase in absorption in the surrounding active layers of the organic solar cells.

For our approach, we use an industrially-applicable method for producing silver nanowires on a large area via filling anodic aluminum oxide (AAO) templates using electrodeposition. AAO was first introduced as a self-organizing mesoporous structure by Keller et al. in 1953.[20] Much research was later conducted to improve the formation and to fabricate AAO pores with various pore distances and diameters using thick (∼ mm) bulk Al foils.[21] Recently, it has been shown that the production of AAO templates on transparent conducting substrates such as ITO glass is also possible. However, due to the chemical instability of ITO,[22] limited work has been performed using ITO substrates as base for the AAO templates. Chu et al.[23,24] initially fabricated AAO templates directly on ITO glass. Unfortunately, this treatment resulted in a spontaneous breakdown of ITO film and delamination of AAO templates. This issue was resolved by Musselman et al.,[25] who overcame these problems by inserting adhesive layers (W and Ti), allowing for the fabrication of large-area free-standing Ni, Cu, Cu_2O and TiO_2 nanowire arrays. However, fabricating large-area Ag nanowire arrays on ITO glass has been a great challenge, due to poor nucleation on both the pure and W/Ti modified surfaces, resulting in extremely uneven filling of the template.

In this work, we have found that the Ag nanowire arrays can be achieved by adding an in situ oxygen plasma process and a Ti layer to enhance the adhesion between the AAO template and the ITO glass, and by inserting Au as a nucleation layer. First, we demonstrate the fabrication of AAO templates on ITO glass (with Ti and Au layers) and examine the influence of the anodizing voltage. Second, the pulsed electrodeposition of Ag nanowire arrays is discussed in detail. Finally, we display the tunable plasmon resonance effects of Ag nanowire arrays, indicating that by changing the dimension of such nanostructures, light can be effectively manipulated.

Experimental

Sputter deposition.—Commercial ITO substrates (Praezisions Glas & Optik) consist of a 180 nm thick ITO layer (∼10 Ω sq^{-1}) deposited on soda-lime-silica glass (14 × 14 × 1.1 mm). The substrates were first cleaned with dishwashing detergent, and then in an ultrasonic bath for 10 min each with acetone and isopropanol prior to loading in the sputtering system. The sputtering system equipped with in situ oxygen plasma cleaning capabilities (AJA Orion 5) was pumped down to 2×10^{-7} Torr. The ITO substrates were exposed to oxygen plasma for 2 min at an oxygen flow rate, power, and pressure of 15 sccm, 50 W and 10 mTorr, respectively. This cleaning process is crucial for enhancing the adhesion between ITO and subsequent layers. 99.95% pure Ti (5 nm) and Au (2 nm) (AJA International, Inc) were sputtered at a rate of 0.20 nm/s and 0.75 nm/s, respectively without breaking chamber vacuum. The RF deposited Ti was sputtered at a power and argon pressure of 100 W and 2 mTorr while the Au was sputtered under direct current (DC) at a power and argon pressure of 20 W and 1.5 mTorr. The samples were subsequently taken out of the aforementioned sputtering system and transferred into the load lock

*Electrochemical Society Student Member.
[z]E-mail: yuyi.feng@uni-konstanz.de; lukas.schmidt-mende@uni-konstanz.de

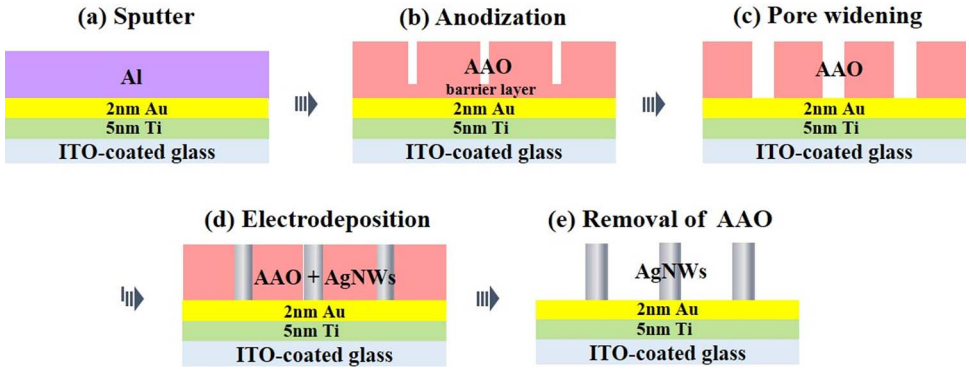

Figure 1. Free-standing silver nanowire fabrication scheme.

chamber of another sputtering system (Surrey NanoSystems Gamma 1000C). The samples were degassed at 200°C for 5 min at approximately 10^{-5} Torr and allowed to cool to room temperature prior to the Al sputtering. This degassing process was used to remove the moisture bonded on the sample surface due to breaking the vacuum. High-purity aluminum (99.999%, Testbourne Ltd.) (150 nm) was DC sputtered at a power and argon pressure of 200 W and 5 mTorr at a rate of 0.05 nm/s. All sputter processes were performed at room temperature.

Anodization and pore widening.—Anodization was carried out at 5°C using a two electrode system in a jacketed beaker cooled by a recirculating chiller. The samples were installed in a homemade leakage-free Teflon holder with an O-ring sealed window exposing the center of the sputtered Al surface (1.27 cm^2) to the 0.1 M oxalic acid (Sigma-Aldrich). The samples were contacted with four gold pins, one at each corner. A Keithley 2400 SourceMeter supplied the constant anodizing potential, and a platinum wire ring counter electrode was placed in parallel to the Al film at a distance of 1–2 cm. The current was monitored throughout the anodization process by a LabVIEW program. As the pores reached the bottom of the Al, the sample turned transparent. When vigorous gas bubbles uniformly spread out from the sample surface, the anodization was manually stopped. It is important to stop the anodization process at the proper point because the barrier layer needs to be thinned for a sufficient duration, but the process should not be too long as this would damage the film. The alumina barrier layer was subsequently completely removed in 5 wt% phosphoric acid (Sigma-Aldrich) at room temperature while the AAO pores widened.

Electrodeposition and the removal of the AAO templates.—The pulsed electrodeposition was performed in a three-electrode system with an Autolab PGSTAT 101 potentiostat/galvanostat. The electrolyte solution was prepared using 50 ml of 0.05 M silver sulfate (Sigma-Ag_2SO_4; Aldrich) and 2.3 M potassium thiocyanate (KSCN; Sigma-Aldrich) in deionized water (pH 6.0). The pH of the solution was then adjusted to 4.2 by adding 40 ml acidic buffer 0.2 M monopotassium phosphate (KH_2PO_4; Sigma-Aldrich). Then, 20 ml of methanol was slowly added to the solution as a wetting agent. Finally, the pH of the solution was stabilized to 6.0 with 7 ml alkaline buffer 0.2 M dipotassium phosphate (K_2HPO_4; Sigma-Aldrich). The ratio of water to methanol was about 1:5. The solution was stirred throughout the preparation process. The AAO samples were electrically connected as before in the leakage-free Teflon holder. An Ag/AgCl (3 M NaCl) electrode was used as a reference and a 2.25 cm^2 platinum counter electrode was employed. For pulse deposition, the following parameters were used: deposition voltage $U_{pulse} = -0.5$ V, pulse time $t_{pulse} = 6$ ms, relaxation voltage $U_{off} = -0.157$ V and relaxation time $t_{off} = 1$ s.

The AAO templates were removed by etching in 0.1 M sodium hydroxide (NaOH; Sigma-Aldrich) for 30 min at room temperature. Subsequently, the samples were cleaned in deionized water, and dried carefully with slight nitrogen flow. Hence, the free-standing Ag nanowire arrays on ITO glass were obtained.

Structural characterization.—The nanowire arrays were characterized using a scanning electron microscope (SEM) (Zeiss Neon 40EsB) operated at 5 keV. X-ray diffraction was performed on a Bruker AXS D8 Advance diffractometer using CuKα radiation and a grazing incidence mode.

Optical measurements.—The absorption spectra were performed in a double beam Cary 5000 series UV-vis-NIR spectrometer (Agilent Technologies). Samples were installed on a rotating stage and placed in the center of an integrating sphere (150 mm diameter), which eliminates the influence of scattering, with a direct measurement of absorbance, rather than extinction. The absorption is determined by detecting the total reflection and transmission through the sample. The beam size on the sample was approximately 6.25 mm^2, adjusted by appropriate lenses. The absorption spectra were scanned from 800 to 300 nm at a rate of 1 nm/s, a spectral bandwidth of 5 nm, and were referenced to 100% and 0% transmittance.

Results and Discussion

AAO template.—Figures 1a–1c show the fabrication scheme of AAO templates on ITO glass. 5 nm of Ti as an adhesive layer, 2 nm of Au and 150 nm of Al were deposited on ITO glass by sputtering. The in situ oxygen plasma pre-cleaning of the ITO surface was found to be crucial for preventing the template from peeling off during the anodization process; high vacuum was maintained between the pre-cleaning and the subsequent layer depositions. Sputtering parameters specific to the system used are displayed in the Experimental section. The ultrathin transparent Au layer is not a continuous film but rather Au dots uniformly distributed over the ITO surface (see Figure S1 in Supporting Information). These Au dots are essential in providing nucleation sites for the silver electrodeposition. Without the use of this Au seed layer, there were only sparse Ag nuclei when directly deposited on the low-surface-energy[26] ITO film. Other attempts at electrodepositing Ag on WO_3, Cr, Ti and amorphous TiO_2 films did not yield homogenous nanowire growth, possibly due to large lattice mismatches (more than 8%, while only 0.3% between Au and Ag).

Figure 2 shows a detailed plot of current density versus time (J-t) for the anodization at 60 V in 0.1 M oxalic acid. 0.1 M oxalic acid is used in this study instead of the more common 0.3 M oxalic acid[25] since the anodization process is too fast to stop in time when using the more concentrated acid for anodizing thin Al film. During the first few seconds, a high current is detected while the surface of Al is oxidized. The current swiftly drops to a local minimum once the oxide layer is completely formed (1). The pores start to form due to local electric field enhancement induced by film roughness and cracks

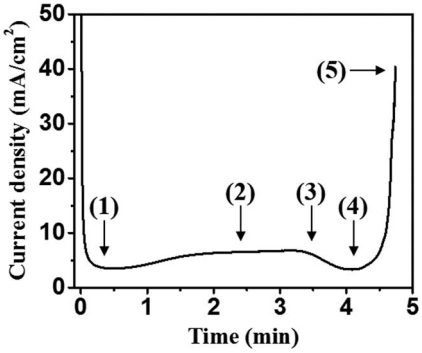

Figure 2. Current density vs. time curve for the anodization at 60 V of a 150 nm Al on ITO glass (with 5 nm Ti and 2 nm Au layers) in oxalic acid (0.1 M). (1–5) label different stages of the anodization process as discussed in the text.

in the oxide layer.[25] The current increases during the progression of the pores through the Al film (2).

The subsequent significant current drop (3) is ascribed to a complete consumption of Al, first locally, and finally over the whole substrate, leaving an Al_2O_3 barrier layer at the bottom of the pores. At this point, the current reaches a local minimum (4). At the end of the anodization process, the current rapidly increases, accompanied by vigorous gas bubbles (5). These gas bubbles are likely due to the oxidation of O^{2-} ions, which migrate through the porous alumina barrier to the Au interface.[23] It is critical to stop the current at the proper point, because stopping too late would cause delamination of the template due to the pressure produced by the gas bubbles. However, since this process also thins the barrier layer underneath of the pores,[23] stopping too early leaves too thick of a barrier layer to be removed by 5 wt% phosphoric acid, one example of which can be seen in Figure S2 in Supporting Information. Such an insulating barrier layer severely blocks the electron pathways to the conducting substrates, leading to failure of electrodeposition of nanowires.

Figure 3a shows a SEM image of an AAO template made by anodizing 150 nm Al on ITO glass at 60 V, followed by 80 min of pore widening. The inset shows the pore diameter distribution, examined by ImageJ software. The AAO template is uniform on the whole substrate (with an area of 1.27 cm^2). To identify the stability of the ITO film in the anodization process, the sheet resistance was characterized by a four-point probe after removing the AAO template in NaOH (0.1 M) for 30 min. There was no significant change

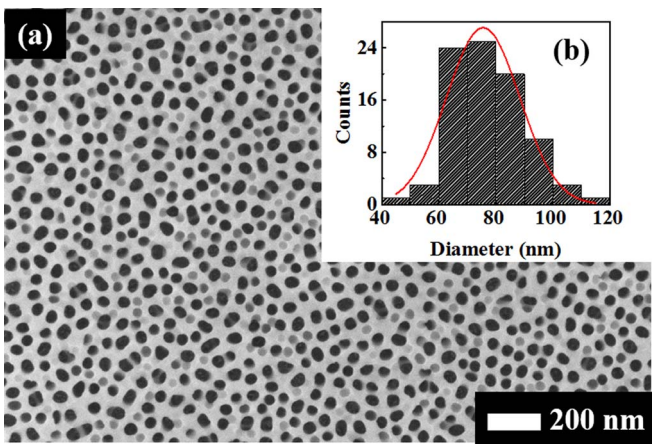

Figure 3. (a) SEM image of an AAO template on an ITO glass substrate (with 5 nm Ti and 2 nm Au layers) by anodization in oxalic acid (0.1 M) at 60 V and pore-widening in 5 wt% phosphoric acid for 80 min. (b) Pore diameter distribution; average pore diameter = 76 ± 13 nm, inter pore distance = 133 ± 15 nm and porosity = 5.5 × 10^9 cm^{-2}.

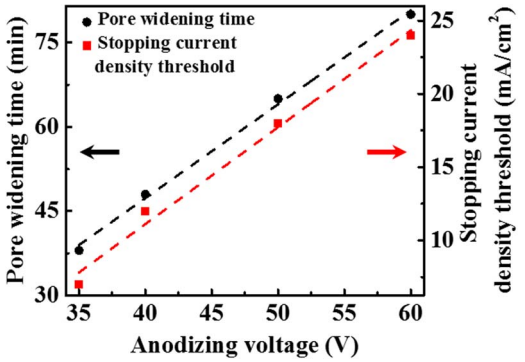

Figure 4. Pore widening time and stopping current density at different anodizing voltages.

between the remaining ITO (7.1 Ω sq^{-1}) and the pristine ITO film (6.9 Ω sq^{-1}).

Different voltages were used to anodize Al films to investigate the influence of this parameter. The stopping current density thresholds and pore widening times at different anodizing voltages (35 V, 40 V, 50 V and 60 V) are plotted in Figure 4 and summarized in Table I. These AAO pores were widened for a sufficient time such that the barrier layers at the bottoms were totally removed. Figure 4 shows that the stopping current density threshold and pore widening time are linearly dependent on the anodizing voltage. Since the barrier layer thickness linearly increases with respect to increasing anodizing voltage,[27] higher electric currents to reduce the barrier layer thickness and longer pore widening times to completely open the bottom of the pores are required. This linear relationship can help determine the stopping current density (see Equation 1) and pore widening time (see Equation 2) at any anodizing voltage within the working range of the oxalic acid.

$$y_{SJ} = 0.66x - 15.32 \quad [1]$$

$$y_{PW} = 1.67x - 19.54 \quad [2]$$

where x is the anodizing voltage, y_{SJ} is the stopping current density threshold and y_{PW} is the minimum pore widening time to completely remove the barrier layer. The interpore distance and widened pore diameter at different anodizing voltage are examined from the SEM images (see Figures S3 in Supporting Information), and summarized in Table I. It is found that the interpore distance depends linearly on the anodizing voltage with a proportionality constant of 1.9 nm/V. This agrees well with the reported data on conventional anodizing of bulk Al foils.[28]

However, the success rates of AAO templates formed at different anodizing voltages are not the same. At lower anodizing voltages, delamination of AAO film was occasionally observed. Higher anodizing voltages make the AAO formation process faster and reduce the occurrence of defects.[29] At 35 V to 40 V, the success rate was below 45%, whereas it increased to over 85% at 50 V to 60 V.

Silver nanowires.—Figures 1d–1e illustrate schematically the electrodeposition of silver into the AAO templates and the removal of AAO templates to get free-standing Ag nanowires.

Table I. AAO template parameters at different anodizing voltages.

Anodizing voltage (V)	Stopping current density threshold (mA cm^{-2})	Pore widening time (min)	Interpore distance (nm)	Pore diameter (nm)
35	7	38	84 ± 13	38 ± 3
40	12	48	96 ± 19	56 ± 13
50	18	65	112 ± 8	70 ± 5
60	24	80	133 ± 15	76 ± 13

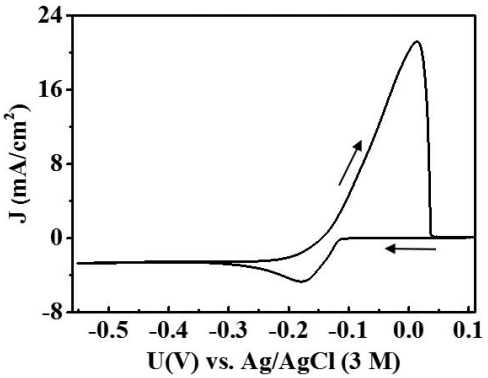

Figure 5. Cyclic voltammetry of a gold electrode in the silver electrodeposition bath scanned from 0.1 V to −0.55 V. Scan rate: 10 mV s^{-1}. The anodic to cathodic charge ratio is 0.8704.

Pulsed electrodeposition of silver was performed using a standard three-electrode system. To achieve uniform pore filling of Ag into the AAO pores, it is critical to choose a suitable electrolyte. Since cyanide electrolytes are not stable in acidic conditions, most traditional cyanide-based silver electrolytes are set to operate at pH > 10.0.[30] However, AAO templates are only stable at a pH between 4.0 and 8.0.[31] Considering the toxicity and poor compatibility with the AAO templates, it was necessary to develop a cyanide-free electrolyte. Our previous attempts at using silver nitrate solutions were unsatisfactory as they resulted in poorly electroformed dendritic silver. Therefore, we chose to use a silver complex solution to obtain fine-grained and smoother Ag. We used the recipe based on the experiment of Riveros et al.,[32] using Ag_2SO_4 as the silver ion source and KSCN as the complex ligand. To facilitate wetting of the AAO pores during the electrodeposition, we added methanol to aqueous solution. The pH of the electrolyte is stabilized at 6.0 with a K_2HPO_4/KH_2PO_4 (aq) buffer. This solves the problem of the decreasing pH, which was accompanied by a change in color of the solution during the electrodeposition demonstrated in the work by Riveros et al.[32] Stability of the electrolyte was tested by depositing Ag into about 200 pieces of our AAO templates over a month. In these experiments, there was no apparent degradation or color change in the electrolyte and no obvious differences in the silver deposition.

Cyclic voltammetry is first performed on a flat gold film (30 nm Au on a silicon substrate) to determine the silver electrodepositing potential range, as shown in Figure 5. It exhibits only one redox reaction in the potential range of −0.55 V to 0.1 V and the deposition peak for silver is −0.18 V. The anodic to cathodic charge ratio was close to 1, irrespective of the number of cycles. All potentials presented regarding electrodeposition in this paper are with respect to the Ag/AgCl (3 M NaCl) reference electrode.

The pulsed electrodeposition of Ag into AAO pores is composed of modulated pulses in milliseconds ($U_{pulse} = -0.5$ V, $t_{pulse} = 6$ ms). An overpotential of −0.5 V was required instead of −0.18 V, because the bottoms of the AAO templates are more likely mesoporous alumina rather than fully exposed gold, which leads to higher resistivity than a pure gold layer. Therefore also the cyclic voltammetry curve is shifted for AAO templates with a bottom layer of gold compared to planar gold films. A relatively long relaxation period subsequently takes place ($t_{off} = 1$ s) with zero current at an offset voltage applied of $U_{off} = -0.157$ V. We adopt a pulsed electrodeposition concept here for two reasons. First, it has been shown that the pulsed electrodeposition can help achieve uniform and homogenous pore filling since a sufficient relaxation period assists the recovery of the silver ion concentration at the deposition interface.[33] Second, since the silver electrodeposition rate is very high, to obtain short nanowires, the relaxation period of pulsed deposition can slow down the whole process. It is important to point out that prior to electrodeposition, the AAO templates are transparent. After electrodeposition, the surfaces turn colorful (from brownish to purplish with increasing the electrodeposition time). However, if the electrodeposition time is too long, the surfaces turn whitish, due to strong light scattering at the overgrown microstructured film. This change in the appearance of the surface of the AAO templates can be used to determine when a sufficient amount of silver has been deposited.

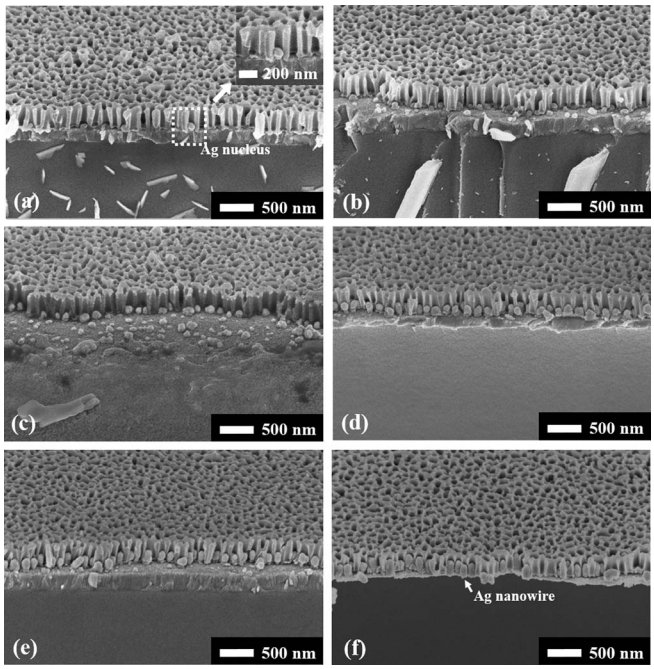

Figure 6. SEM side views of electrodeposited silver nanostructures into AAO templates, anodized at 60 V, with an average diameter of 76 nm and interpore distance of 133 nm. The electrodepositing times and charges are: a) 5 s, 1.58 mC, b) 10 s, 6.75 mC, c) 15 s, 10.95 mC, d) 22 s, 33.64 mC, e) 30 s, 47.01 mC, and f) 45 s, 59.85 mC. The stage angle is 54°.

The crystal growth of the Ag nanowire arrays is supported in the X-ray diffraction (XRD) (see Figure S4 in Supporting Information). The pattern shows the expected reflections for the silver material. Comparing the relative intensities of the silver reference pattern, one can conclude that the growth of Ag nanowires was successful.

Figures 6a–6f display side view SEM images of the well-controlled different lengths of the Ag nanowires embedded in the AAO templates on ITO glass with increasing electrodeposition time from 5 s to 45 s. At times shorter than 10 s, only a few Ag nuclei are observed as opposed to nearly full coverage after this critical time. Afterwards, the Ag uniformly deposits in the AAO pores resulting in Ag nanowires. All of the AAO templates discussed in this section are anodized at 60 V, with an average diameter of 76 nm and an average interpore distance of 133 nm.

A prolonged current density versus time (J-t) pulsed electrodeposition curve is recorded, shown in Figure 7. The inset side view SEM image displays the severe overgrowth of Ag nanowires. In the J-t curve, there are three main stages: I) transient stage for Ag nucleation; II) steady stage for Ag growing in the pores; III) increasing stage when hemispherical Ag caps start forming. This agrees with previously reported work of electrodeposition of metal nanowires into polycarbonate membranes.[34] The process should be stopped at the transition point between stage II and III to obtain homogenous silver nanowires as overgrowth starts to dominate.

The length of the high-quality Ag nanowires, examined from the side view SEM images of the samples, is linearly dependent on the charge collected on the sample, as shown in Figure 8a. This agrees well with the Faraday's law[35] and proves a uniform nanowire growth under the applied electrodeposition conditions. Since only a small portion of AAO pores are filled with Ag at the beginning of the electrodeposition,

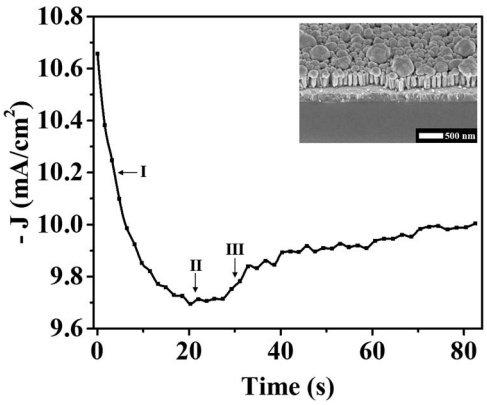

Figure 7. Current density vs. time curve for pulsed electrodeposition of silver into AAO templates on ITO glass. It displays the recorded data when the pulse is on, which mainly determines the silver nanowire growth.

which is seen from the SEM image (Figure 6a), the examined length here is the average value of these few Ag nuclei. Therefore, the linear mapping starts at approximately 90 nm rather than 0 nm. In addition, this linear mapping can in turn be used to estimate the length of the Ag nanowires of good quality. Note that the same length of Ag nanowires is not necessarily obtained with the same electrodeposition time, since the current density always changes with different samples due to the inevitable fluctuations at the bottom of the AAO pores.

In rare cases, overgrowth of Ag nanowires happens even when the average length of the Ag nanowires is still short. This is undesirable for certain device fabrications such as organic and hybrid solar cells because it causes an electrical short-circuit between the two electrodes. One poor quality Ag nanowire sample is presented in Figure 8a, which does not fit the linear relationship of nanowire length and deposited charge. Its side view SEM image is displayed in Figure 8b. It is assumed that this inhomogeneous overgrowth is due to the uneven barrier layer at the bottom of the AAO pores. Hence, homogenous

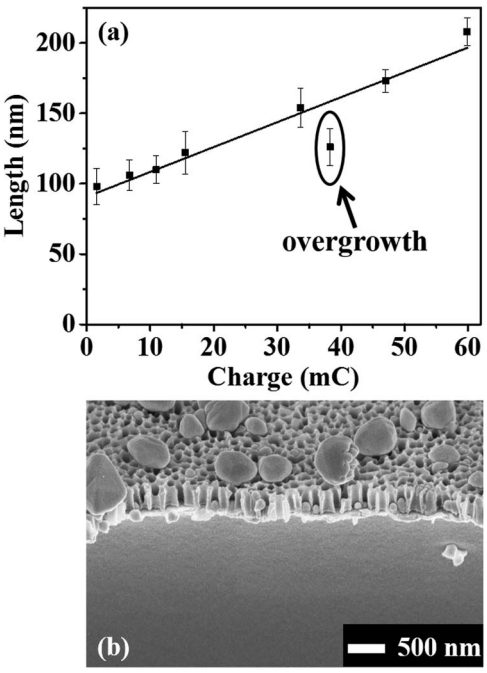

Figure 8. (a) Mean and standard deviation of the silver nanowires length with respect to the charge collected on the samples. The straight line represents a linear fit to the data. (b) A side view SEM image of one overgrown silver nanowire sample embedded in the AAO template.

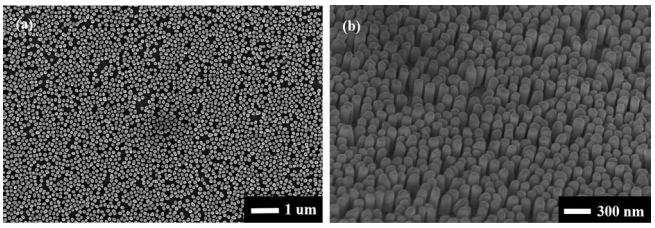

Figure 9. SEM images of free-standing silver nanowires on ITO glass substrates: (a) top view, (b) side view at an angle of 54°.

barrier layer quality of AAO templates is essential for uniform pore filling.

Figures 9a–9b display SEM images of the samples after removal of the AAO templates. The high quality of the Ag nanowires is shown in the lower magnification image of Figure 9a. The 90 μm^2 area is uniform and free of collapsed nanowires, and is representative of the entire 1.27 cm^2 sample area.

Figure 10 shows the absorbance for different lengths of Ag nanowire arrays at an incident angle of 25°. For each length of the Ag nanowire arrays, there are two distinct peaks: one is at the shorter wavelength and is related to transverse resonance of the Ag nanowires; the other is at the longer wavelength and is associated with the longitudinal axis of the Ag nanowires.[36] With diameter remaining almost constant, the transversal peak stayed nearly the same at ~370 nm. However, with length increasing from 183 nm to 212 nm, the longitudinal peak redshifts considerably by 52 nm and its absorbance decreases by 20%. This reduction in absorbance for the 212 nm nanowires is expected to originate from the lower AgNW density in comparison to the 183 nm nanowires. This indicates that by changing the dimension of the silver nanowires, the resonance peaks can be tuned in the UV-Vis range to, for example, meet the demands of enhancing the electromagnetic field at specific wavelengths in surface-enhanced Raman scattering (SERS) substrate, biosensing and solar cells.

Conclusions

Uniform large-area free-standing Ag nanowire arrays on ITO glass have been reproducibly fabricated by a combined technique of thin film aluminum anodization and pulsed electrodeposition. In situ oxygen plasma cleaning of the ITO surface and the sputtered Ti layer provide excellent adhesion during the anodization process. The ultrathin gold layer is found to be a desirable nucleation layer for the electrodeposition of Ag. The diameter of the Ag nanowires (38–80 nm), and the separation between them (84–133nm) can be controlled

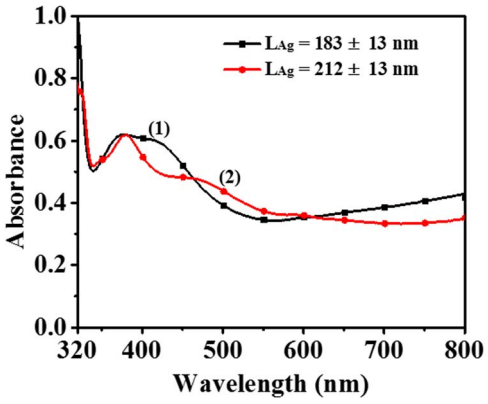

Figure 10. Absorption spectra at an incident angle of 25° of free-standing Ag nanowires with diameter = 76 ± 13 nm, interpore distance = 133 ± 15 nm. (1) length = 183 ± 13 nm, aspect ratio = 2.2, (2) length = 212 ± 13 nm, aspect ratio = 2.6.

by the AAO template. The length can be estimated from the linear curve of the length versus collected charge. The Ag nanowire arrays present tunable plasmon resonance effects in the UV-Vis region, and such nanostructures can be useful in the applications for SERS substrate, biosensing, electrodes for photoelectric devices, and many others.

Acknowledgments

Y. F. acknowledges the China Scholarship Council for support. K. D. K. acknowledges the Basic Science Research Program through the National Research Foundation of Korea funded by the Ministry of Education, Science and Technology (No. NRF-2013R1A6A3A03057669), and the REFINE research consortium of the Carl Zeiss Foundation. J. A. D. acknowledges the Alexander von Humboldt Foundation for support through a postdoc fellowship. J. W. acknowledges funding by the Carl Zeiss Foundation through a postdoc fellowship. The authors thank Prof. Ting Zhang, Torsten Pietsch, Liangfei Tian, Bingqiang Lu, Sergej Andreev and Stefan Scheerer for valuable discussions, Matthias Hagner, Hao Chen and Hamidreza Riazi-Nejad for technical support, and Prof. John Mathis for proofreading.

References

1. Z. Fan, H. Razavi, J.-w. Do, A. Moriwaki, O. Ergen, Y.-L. Chueh, P. W. Leu, J. C. Ho, T. Takahashi, L. A. Reichertz, S. Neale, K. Yu, M. Wu, J. W. Ager, and A. Javey, *Nat. Mater.*, **8**(8), 648 (2009).
2. T. Pfadler, M. Coric, C. M. Palumbiny, A. C. Jakowetz, K.-P. Strunk, J. A. Dorman, P. Ehrenreich, C. Wang, A. Hexemer, and R.-Q. Png, *ACS nano*, **8**(12), 12397 (2014).
3. J. J. Hill, N. Banks, K. Haller, M. E. Orazem, and K. J. Ziegler, *J. Am. Chem. Soc.*, **133**(46), 18663 (2011).
4. K. P. Musselman, A. Marin, A. Wisnet, C. Scheu, J. L. MacManus-Driscoll, and L. Schmidt-Mende, *Adv. Funct. Mater.*, **21**(3), 573 (2011).
5. M. E. Nasir, W. Dickson, G. A. Wurtz, W. P. Wardley, and A. V. Zayats, *Adv. Mater.*, **26**(21), 3532 (2014).
6. M. M. Maqableh, X. Huang, S.-Y. Sung, K. S. M. Reddy, G. Norby, R. Victora, and B. J. Stadler, *Nano Lett.*, **12**(8), 4102 (2012).
7. N. Vasilantonakis, M. E. Nasir, W. Dickson, G. A. Wurtz, and A. V. Zayats, *Laser Photon. Rev.*, **9**(3), 345 (2015).
8. S. J. Lee, A. R. Morrill, and M. Moskovits, *J. Am. Chem. Soc.*, **128**(7), 2200 (2006).
9. S. Parkin and S.-H. Yang, *Nat. Nanotechnol.*, **10**(3), 195 (2015).
10. A. W. Maijenburg, J. Veerbeek, R. de Putter, S. A. Veldhuis, M. G. C. Zoontjes, G. Mul, J. M. Montero-Moreno, K. Nielsch, H. Schafer, M. Steinhart, and J. E. ten Elshof, *J. Mater. Chem. A*, **2**(8), 2648 (2014).
11. G. Zheng, F. Patolsky, Y. Cui, W. U. Wang, and C. M. Lieber, *Nat. Biotechnol.*, **23**(10), 1294 (2005).
12. L. Schmidt-Mende and J. L. MacManus-Driscoll, *Mater. Today*, **10**(5), 40 (2007).
13. J. Weickert, R. B. Dunbar, H. C. Hesse, W. Wiedemann, and L. Schmidt-Mende, *Adv. Mater.*, **23**(16), 1810 (2011).
14. E. C. Garnett, M. L. Brongersma, Y. Cui, and M. D. McGehee, *Annu. Rev. Mater. Res.*, **41** 269 (2011).
15. N. O. Plank, H. J. Snaith, C. Ducati, J. S. Bendall, L. Schmidt-Mende, and M. E. Welland, *Nanotechnology*, **19**(46), 465603 (2008).
16. L. E. Greene, M. Law, B. D. Yuhas, and P. Yang, *J. Phys. Chem. C*, **111**(50), 18451 (2007).
17. A. Wisnet, K. Bader, S. B. Betzler, M. Handloser, P. Ehrenreich, T. Pfadler, J. Weickert, A. Hartschuh, L. Schmidt-Mende, and C. Scheu, *Adv. Funct. Mater.*, **25**(17), 2601 (2015).
18. J. A. Dorman, J. Weickert, J. B. Reindl, M. Putnik, A. Wisnet, M. Noebels, C. Scheu, and L. Schmidt-Mende, *J. Phys. Chem. C*, **118**(30), 16672 (2014).
19. R. B. Dunbar, T. Pfadler, N. N. Lal, J. J. Baumberg, and L. Schmidt-Mende, *Nanotechnology*, **23**(38), 385202 (2012).
20. F. Keller, M. S. Hunter, and D. L. Robinson, *J. Electrochem. Soc.*, **100**(9), 411 (1953).
21. H. Masuda, H. Yamada, M. Satoh, H. Asoh, M. Nakao, and T. Tamamura, *Appl. Phys. Lett.*, **71**(19), 2770 (1997).
22. J. J. Hill, K. Haller, and K. J. Ziegler, *J. Electrochem. Soc.*, **158**(1), E1 (2011).
23. S. Z. Chu, K. Wada, S. Inoue, and S. Todoroki, *J. Electrochem. Soc.*, **149**(7), B321 (2002).
24. S.-Z. Chu, K. Wada, S. Inoue, S.-i. Todoroki, Y. K. Takahashi, and K. Hono, *Chem. Mater.*, **14**(11), 4595 (2002).
25. K. P. Musselman, G. J. Mulholland, A. P. Robinson, L. Schmidt-Mende, and J. L. MacManus-Driscoll, *Adv. Mater.*, **20**(23), 4470 (2008).
26. H. P. Feng, T. Paudel, B. Yu, S. Chen, Z. F. Ren, and G. Chen, *Adv. Mater.*, **23**(21), 2454 (2011).
27. K. Ebihara, H. Takahashi, and M. Nagayama, *J. Met. Finish. Soc. Jpn.*, **34**(11), 548 (1983).
28. L. Zaraska, G. D. Sulka, J. Szeremeta, and M. Jaskuła, *Electrochim. Acta*, **55**(14), 4377 (2010).
29. T. R. B. Foong, A. Sellinger, and X. Hu, *ACS Nano*, **2**(11), 2250 (2008).
30. M. Schlesinger, *Electroless and electrodeposition of silver*, John Wiley (2010).
31. C.-N. Yeh, K. Raidongia, J. Shao, Q.-H. Yang, and J. Huang, *Nat. Chem.*, **7**(2), 166 (2015).
32. G. Riveros, S. Green, A. Cortes, H. Gomez, R. E. Marotti, and E. A. Dalchiele, *Nanotechnology*, **17**(2), 561 (2006).
33. K. Nielsch, F. Müller, A. P. Li, and U. Gösele, *Adv. Mater.*, **12**(8), 582 (2000).
34. T. M. Whitney, P. C. Searson, J. S. Jiang, and C. L. Chien, *Science*, **261**(5126), 1316 (1993).
35. I. U. Schuchert, M. E. Toimil-Molares, D. Dobrev, J. Vetter, R. Neumann, and M. Martin, *J. Electrochem. Soc.*, **150**(4), C189 (2003).
36. P. R. Evans, R. Kullock, W. R. Hendren, R. Atkinson, R. J. Pollard, and L. M. Eng, *Adv. Funct. Mater.*, **18**(7), 1075 (2008).